International Journal of Rock Mechanics & Mining Sciences 188 (2025) 106076

Contents lists available at ScienceDirect

International Journal of Rock Mechanics and Mining Sciences

journal homepage: www.elsevier.com/locate/ijrmms

Influence of roughness and slip velocity on the evolution of frictional strength

Quan Gan [a,b], Xinyuan Zhang [a,b], Qiang Li [a,b], Jianye Chen [c,*], Fengshou Zhang [d], Zhen Zhong [e], Yunzhong Jia [a,b], Pengliang Yu [f], Mengke An [g], Derek Elsworth [f,**]

[a] State Key Laboratory of Coal Mine Disaster Dynamics and Control, Chongqing University, Chongqing, China
[b] School of Resources and Safety Engineering, Chongqing University, Chongqing, China
[c] State Key Laboratory of Earthquake Dynamics, Institute of Geology, China Earthquake Administration, Beijing, China
[d] Department of Geotechnical Engineering, Tongji University, Shanghai, China
[e] School of Civil Engineering, Shaoxing University, Shaoxing, China
[f] Department of Geosciences, Pennsylvania State University, University Park, PA, USA
[g] Department of Civil and Environmental Engineering, The Hong Kong Polytechnic University, Hung Hom, Kowloon, Hong Kong, China

ARTICLE INFO

Keywords:
Sandstone fractures
Frictional healing
Frictional strength
Slide-hold-slide experiments

ABSTRACT

Surface roughness and slip velocity play a critical role in determining the strength of crustal faults and their potential seismic response. We examine these controls through slide-hold-slide (SHS) experiments on bare sandstone fractures of variable roughnesses and slip velocities. These experiments explore the effects of frictional healing and frictional relaxation quantified through rate-and state-dependent friction law (RSF). Frictional healing rates (β) range between 0.0020 and 0.0074 and frictional relaxation rates (β_c) between 0.0058 and 0.0097. Increases in surface roughness and shear velocity each accelerate healing and relaxation, whereas elevated normal stresses promote accelerated healing but suppress relaxation. Fracture contact area is closely correlated with changes in frictional healing rate with the evolution of protrusion playing a key role in this frictional response. The number of time-binned AE ring-down counts increase with increasing strength as observed during reactivation – and therefore serve as a reliable indicator of increased strength gain. The logarithmic relationship between hold-time and evolution in the contact area is confirmed by correlations with seismic moment independently measured from the absolutely calibrated AE data. This correlates with an observed increased RSF-*b* evocative of elevated frictional recovery during hold that translates to a more rapid and intense energy release.

1. Introduction

Fractures and faults as planes of weakness are widespread in the Earth's crust. Sliding or rupture occurs when tectonic stress accumulation is released on these fractures (faults). Such sliding or rupture typically occurs along pre-existing fractures (mature faults) and is often sudden and intense, releasing a substantial amount of energy and thus triggering earthquake.[1–9] In addition to tectonic earthquakes, induced seismicity and fault reactivation have become critical in human activities such as oil and gas extraction, hydraulic fracturing, and geothermal development.[10–16]

Understanding frictional healing behaviour is crucial in understanding the earthquake cycle of pre-existing faults, as frictional strengthening is a prerequisite for the recurrence of earthquakes on the same fault.[17–22] To gain deeper insights into the triggering mechanisms of earthquakes and fault activity during seismic events, we explore this frictional behavior, and in particular, the evolution of frictional strength in the repose period between sliding events. The rate at which a fault recovers the frictional strength lost during shear slip controls the recurrence interval and the maximum strength achievable before the next earthquake. This critical understanding has spawned many laboratory studies to focus on the time dependence of frictional strength.[18,23–26]

Although measuring frictional characteristics under laboratory in situ conditions is challenging, observations indicate that, under specific circumstances, the rate of frictional strengthening measured in the

* Corresponding author.
** Corresponding author.
E-mail addresses: j.chen3@uu.nl (J. Chen), elsworth@psu.edu (D. Elsworth).

https://doi.org/10.1016/j.ijrmms.2025.106076
Received 5 December 2024; Received in revised form 26 January 2025; Accepted 22 February 2025
Available online 26 February 2025

laboratory approximates seismologically determined values.[23,27,28] Slide-hold-slide (SHS) tests are considered a reliable method to simulate the earthquake cycle in nature and are commonly used to evaluate the time dependence of friction.[18,20,29–31]

Various factors, including mineral composition,[32–34] normal stress,[35–37] temperature,[36,38–40] and the presence of water[41,42] influence the frictional healing or relaxation effects of fractures (faults).

Numerous studies have shown that the mineral composition of fault gouge plays a crucial role in controlling the rates of frictional strengthening, creep relaxation, fault zone dilation, and fault healing.[34,43–48] Specifically, fault gouges rich in phyllosilicates typically exhibit low strength and slow healing characteristics, promoting stable, aseismic creep; most natural fault gouges display moderate frictional strengthening rates consistent with widespread fault slip behaviour; and fault rocks rich in calcite exhibit the highest frictional strengthening rates, low re-shear dilation rates, and high frictional strength, all of which contribute to seismic behaviour.[34]

The rate of frictional healing exhibits a complex dependence on normal stress. Experiments on shale and calcite mixed fault gouge under normal stress conditions ranging from 30 to 100 MPa[49] show that the frictional healing rate in dry laboratory samples increased slightly with applied normal stress. However, the opposite trend was observed for wet 100 % calcite samples, with the healing rate decreasing as normal stress increased.

Frictional healing lacks a clear correlation with temperature, which may be because prolonged static contact or elevated temperatures might activate other healing processes independent of effective normal stress, such as neck growth driven by capillary phenomena or cementation caused by the influx of supersaturated solutions.[36]

Water enhances frictional healing, likely due to fluid-assisted mass transfer promoting increased healing in fault gouges.[50,51] Conversely, water interacts with wear debris generated by sliding, resulting in cementation that temporarily increases the frictional strength of the fracture (strength healing), which is more pronounced in wet samples than dry. However, this cementation is destroyed when the fracture re-activates, causing the frictional strength to eventually stabilize at a new steady state. Conversely, water flow can transport wear debris within the fracture, weakening the cementation, so as the flow rate increases, the amount of frictional healing decreases slightly instead of increasing.[52]

Sandstone, characterized by its high porosity and permeability, is commonly serves as a reservoir for oil and gas,[53,54] groundwater[55,56] and CO_2 geological storage.[57] Previous studies have predominantly focused on the effects of mineral composition, normal stress, temperature and the presence of water on frictional healing, with velocity dependence primarily analyzed in terms of frictional stability.[42,58–60] Research on the effects of shear velocity and frictional healing on frictional strength, as well as the methods for studying fracture surface changes and actual contact area during the friction process, remains limited.

We conducted a series of slide-hold-slide tests on sandstone fractures under varying conditions of fracture roughness (JRC = 1.49, 3.05, 11.72), normal stress (σ_n = 20, 30, 40 MPa), and slip velocity (v = 1, 3, 10 μm/s) to better understand the coupled effects of compaction, shear dilation, and roughness on frictional healing and relaxation. We use bare fractures rather than gouge, emblematic of immature faults, specifically to understand controls of evolving contact area as an anticipated key control.

2. Experimental methods

2.1. Sample preparation and surface characterization

The sandstone samples were obtained from Sichuan Province with mineral compositions identified using X-ray diffraction (XRD). As shown in Fig. 1(a), the sandstone samples were mainly composed of 49.5 % Quartz, 24.5 % Plagioclase, 1.7 % Potassium feldspar, and 24.3 % Clays (of which 8 % were Illite, 29 % Kaolinite, 59 % Chlorite, and 4 % mixed-layer Illite-montmorillonite). Average uniaxial compressive strength is 92.9 MPa and modulus of elasticity (E) 14.3 GPa and Poisson's ratio (ν) 0.27. Samples were sourced from the same single block sample to eliminate compositional and grain size differences. To apply consistent moisture contents, all samples were dried in an oven at 105 °C for 48 h to eliminate the effect of water on the experimental responses.

As shown in Fig. 1(c), the sandstone samples were cored to 50 mm diameter then trimmed to a length of 100 mm. Whereafter, the polished cores were cut into two halves along the axis of the core to form a sandstone fracture. The sawcut surfaces were processed to form fracture surfaces with three different roughnesses. The grinding direction was always perpendicular to the future direction of shear (see Fig. 1(d)).

The roughness of rock fracture surfaces may be characterized through Joint Roughness Coefficient (JRC),[61,62] mathematical-statistical parameters[63,64] or fractal dimension. We quantify surface roughness through 3D topographic optical scanner and calculated to obtain the root mean square of the first-order derivatives of the profile curves (Z_2). The relationship between Z_2 and JRC shown in Equation. (1) was determined statistically through the empirical correlations developed by Tse and Cruden.[63]

$$\begin{aligned} \boldsymbol{Z}_2 &= \sqrt{\frac{1}{\boldsymbol{M}}\sum_{i=1}^{\boldsymbol{M}}\frac{(\boldsymbol{z}_{i+1}-\boldsymbol{z}_i)^2}{(\boldsymbol{x}_{i+1}-\boldsymbol{x}_i)^2}} \\ \boldsymbol{JRC} &= 32.2 + 32.47\ \lg \boldsymbol{Z}_2 \end{aligned} \tag{1}$$

where M is the number of samples taken along the axis, and x_i and z_i are the coordinates of the sampling points on the profile line. To avoid the interference of boundary effect on the calculation results, we use a 40 mm × 80 mm window of the optically profiled surface shown in Fig. 1(b). A total of 80 profile lines were selected along the y direction, with each profile line spaced 0.5 mm apart to obtain Z_2. The average value of Z_2 was used to calculate the JRC value, resulting in JRC values of 11.72, 3.05, and 1.49 for three different roughnesses, respectively-the roughness of each fracture surface was slightly different. The average value was taken as the standard value for comparison.

2.2. Experimental apparatus and procedures

Our experimental design utilized a high-pressure triaxial loading system capable of accommodating the split core samples in shear. The cell uses oil as a confining medium for the triaxial pressure chamber and utilizes two sets of servo control systems for loading and computer control and data acquisition. The servo control systems can apply axial and confining pressures to the sample with a control accuracy of ±0.01 MPa. The deformation measurement device includes two axial linear variable displacement transducers (LVDT) with a resolution of 0.2 μm. The specimen is mounted in the shear device suitable for cylindrical specimens with a diameter of 50 mm. The device is fitted with a cylindrical stepped indenter with a height difference of 8 mm, with the gap between the indenter and the shear-offset specimen filled with an 8 mm thick bed of silicone putty-filler (see Fig. 1(f)). This putty infill allows shortening of the initially shear-offset sample with the applied axial stress, providing negligible additional resistance to axial deformation of the sample.[60] The axial fracture configuration ensures that the normal stress acting on the fracture surface during the test is independent of the shear displacement and is always equal to the confining stress. During the assembly process, a layer of transparent heat shrink tube is used to fix the specimen, indenters, and silicone putty-fillers together to ensure that no positional shift occurs during the loading process. The specimen is then fixed in the core holder with heat shrink tube and secured by sealing clamps on both sides to prevent oil from penetrating during the shear process. The sample loading process and equipment schematic diagram are shown in Fig. 1 (g & h). Additionally, the experiment

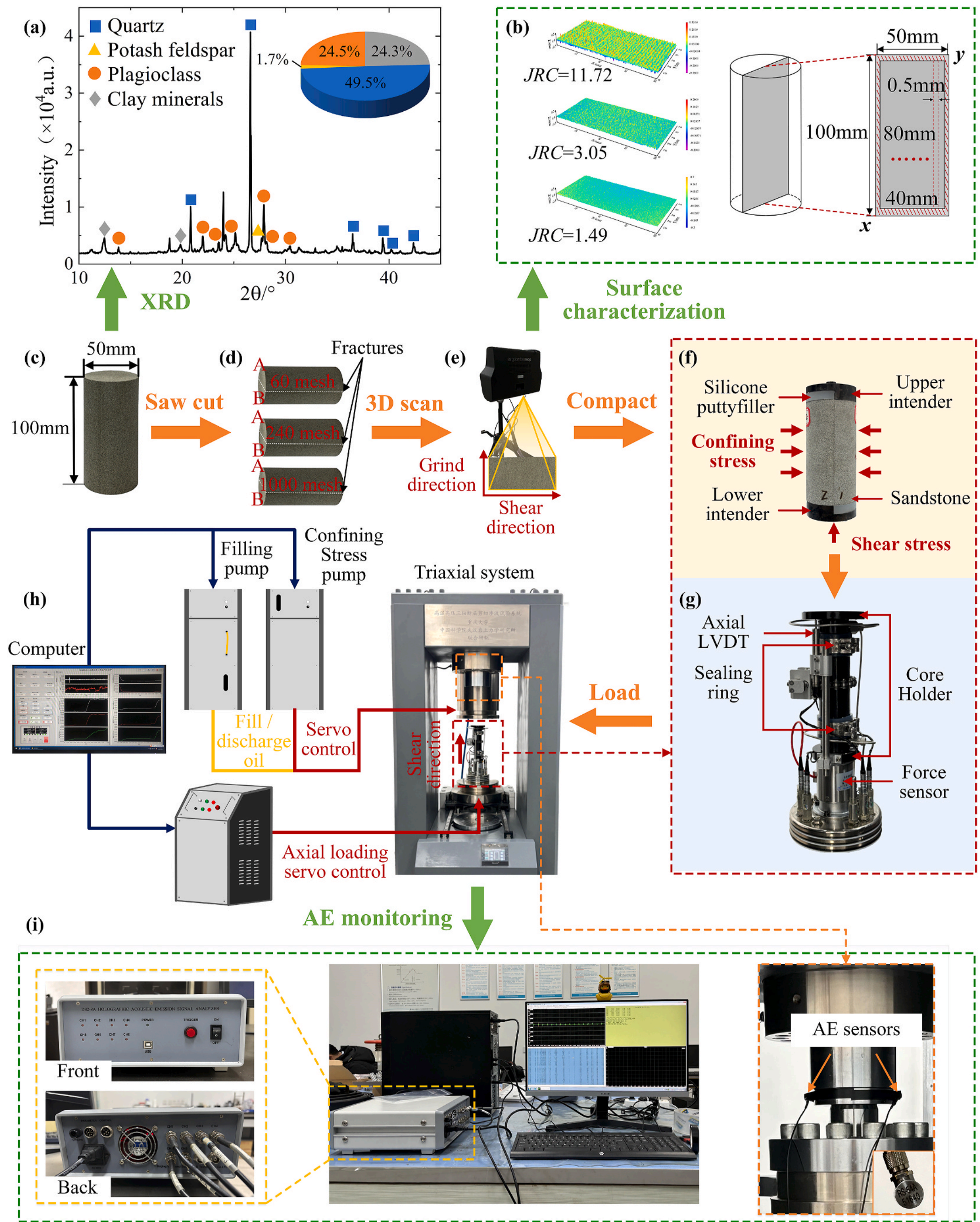

Fig. 1. Schematic of samples and equipment used in the experiments. (a) XRD results on sandstone samples, (b) Reconstruction of fracture surfaces with three different roughnesses and selection of the *JRC* calculation area, (c) Intact sandstone sample, (d) Sandstone fractures with three different roughnesses, (e) 3D scanning of fracture surface morphology, (f) Sample assembly used in the direct shear experiment within the triaxial deformation apparatus, (g) Core holder, (h) High-pressure triaxial fault shear testing system, (i) AE equipment and sensors installation setup.

incorporated a DS2 holographic AE signal analyzer to collect AE signals during the rock shear failure process (see Fig. 1(i)). The AE system has 8 channels, and the AE sensors used are of the DS-54A model, with a threshold set at 40 dB. Due to the sealed nature of the experiment, two AE sensors were mounted on the triaxial apparatus' loading plates for signal collection.

Slid-hold-slide (SHS) tests were conducted to determine the evolution of fracture friction and stability for these different samples and experimental characteristics of surface roughness, normal stresses and shear velocities. To reduce the cross-influence between different factors, each test series controlled a single variable in succession. Only one influencing factor was changed in each group of tests to reduce the interaction among different factors.

For sandstone fractures, a constant target confining pressure (σ_n = 20,30,40 MPa) was first applied. Subsequently, as the 'run-in' stage of all tests, samples with different roughnesses (*JRC* = 11.72,3.05,1.49) were sheared at a constant velocity (v = 1,3,10 μm/s) to steady-state friction. The average displacement of the 'run-in' step was ~1.5 mm. After reaching steady-state frictional strength, shear is arrested and locked before reactivation after the hold period. Hold times were set to 30 s → 100 s → 300 s → 1000 s → 3000 s → 10000 s. The displacement applied for the reactivations between preceding and successive holds is constant at 0.5 mm. Experiments were terminated after total displacements of ~5 mm to prevent slip-induced jacket rupture and reduce geometric effects contributing to stress and/or strain inhomogeneities. All experiments are completed at room temperature with the specific test suite shown in Table 1.

2.3. Parameter definition and analysis

Experimental variables of axial stress, confining stress, and axial (shear) offset were recorded at a frequency of 100 Hz. The raw data were processed to obtain the variation of shear stress τ (MPa) with load point displacement and hold time. Due to the short total slip distances in the tests, the shear stress was calculated based on a constant contact area of 100 mm × 50 mm. The normal stress applied to the sandstone fracture during the test was constant and equal to the value of the confining stress. The impact of cohesion was ignored with frictional strength of the fracture surface characterized by the friction coefficient μ, defined as the ratio of shear stress (τ) to normal stress (σ_n).

Rate-and state-dependent friction law (RSF) constitutive relations are derived from the experimental results of evolution of friction with time/displacement.[65] These equations have been widely applied due to their ability to successfully explain various stages of the seismic cycle, including preseismic slip nucleation,[65] coseismic rupture,[66] aftershocks and postseismic slip,[67] as well as interseismic fault healing.[23,24] As a refinement of Coulomb friction RSF faithfully accommodates important second order variations in friction that contribute to defining the seismic cycle. The general form for RSF is:

$$\begin{aligned} \boldsymbol{\mu} &= \boldsymbol{\mu}_0 + \boldsymbol{a}\ln\left(\frac{\boldsymbol{V}}{\boldsymbol{V}_0}\right) + \boldsymbol{b}\ln\left(\frac{\boldsymbol{V}_0\boldsymbol{\theta}}{\boldsymbol{D_c}}\right) \\ \frac{\boldsymbol{d\theta}}{\boldsymbol{dt}} &= 1 - \frac{\boldsymbol{V\theta}}{\boldsymbol{D_c}} \end{aligned} \tag{2}$$

Temporal evolution is accommodated through a state variable, θ, defined here by the “slowness law”.[68] In this equation, V_0 is the reference velocity, μ_0 is the steady-state friction value at V_0, V is the sliding velocity, and θ is the state variable representing the memory of prior sliding on the contact surface. Thus, the state variable at any given time is influenced by its antecedent value. Parameters a and b are dimensionless constants used to describe the direct and evolutionary effects induced by variations in shear velocity. D_c is the critical slip distance, which is the distance required to transition from steady-state sliding at one velocity to steady-state sliding at another, sometimes viewed as the lifetime of frictional contacts.

Slide-hold-slide experiments were initially conducted by Dieterich[18] to investigate the time dependence of static friction in rock friction experiments. In SHS, steady state sliding is arrested and displacement locked for a set duration – typically lengthening with each successive hold. Post-hold, the velocity is reloaded at the original rate. The change in friction coefficient observed upon reactivation is measured as an indicator of interseismic strengthening. As shown in Fig. 2(a), the shear stress to normal stress ratio (a proxy for friction coefficient) drops gradually during the hold period as the sample relaxes. A new peak friction value is obtained after reloading and is typically higher than the peak friction value recorded in the previous sliding. The increase in the friction coefficient, $\Delta\mu$, is approximately proportional to $\ln t_{\text{hold}}$, indicating a logarithmic relationship between $\Delta\mu$ and t_{hold}. Such measurements are the basis for the evolution equation for the slowness constitutive law. According to the slowness law, when $V = 0$, the state variable θ is linearly related to the hold time t_{hold}, thus, $\Delta\mu$ is proportional to $\ln t_{\text{hold}}$.

The initial steady-state friction value on the fracture surface is defined as μ_{ss}, the minimum friction value during the hold time as $\mu_{\min}$, the maximum friction value achieved after recovery of velocity as μ_{peak}, and the hold time as t_{hold}. The decrease in the friction coefficient during the hold period is defined as the frictional relaxation $\Delta\mu_c$. The difference between the steady-state friction value before the start of the hold and the peak friction value after the hold is denoted as the frictional healing $\Delta\mu$. The values of $\Delta\mu$ and $\Delta\mu_c$ are logarithmically related to t_{hold}, thus defining the frictional healing rate β[19]and the frictional relaxation rate β_c[34] (see Fig. 2(b)) as:

$$\begin{aligned} \boldsymbol{\beta} &= \Delta\boldsymbol{\mu}/\lg \boldsymbol{t_{hold}} \\ \boldsymbol{\beta_c} &= \Delta\boldsymbol{\mu}_c/\lg \boldsymbol{t_{hold}} \end{aligned} \tag{3}$$

Thus, β and β_c are two important parameters reflecting the time dependence of the rock friction coefficient.

3. Results

3.1. Evolution of frictional strength

Fig. 3 shows the variation in friction coefficient with load point displacement during the whole SHS test for different fracture surface roughnesses, normal stresses, and shear velocities. Within this range of parameters, it is evident that roughness and normal stress have a significant influence on frictional strength. As roughness decreases and normal stress increases, friction strength also noticeably decreases and reduces only slightly with a decrease in shearing velocity.

Friction coefficient exhibits an increase in slip-hardening with an increase in load-point displacement; therefore, the friction coefficient at ~3 mm of accumulated shear is taken as the steady-state friction coefficient. As shown in Fig. 4 (a), the friction coefficients of all samples are stable in the range of 0.653–0.751, in accordance with Byerlee’s law.[43]

To quantitatively assess the individual effects of fracture surface roughness (*JRC*), normal stress (σ_n), and shear velocity (v) on the frictional strength, we plot the trend of the frictional strength under the different influencing factors in Fig. 4 (a). Friction coefficient increases by 5.36 % when *JRC* increases from 1.49 to 3.05 and by 4.07 % from 3.05 to 11.72 for $\sigma_n = 40$ MPa and v = 10 μm/s. Conversely, for $JRC = 11.72$ and $v = 10$ μm/s, friction systematically decreases by 1.73 % when σ_n increases from 20 MPa to 30 MPa and by 2.98 % when it increases from 30 MPa to 40 MPa. Similarly, for $JRC = 11.72$ and $\sigma_n = 40$ MPa, the friction coefficient increased by 0.85 % when v was increased from 1 μm/s to 3 μm/s and by 0.7 % when it was increased from 3 μm/s to 10 μm/s. Thus, from these results, it is inferred that fracture roughness had the greatest effect on the frictional strength, followed by normal stress, then shearing velocity.

3.2. Frictional healing and relaxation

Typical results for a hold time of 300 s are highlighted in Fig. 3 (d), depicting the change in the friction coefficient resulting from the transition between sliding and holding and vice versa. The friction coefficient decreases abruptly as the system transitions from sliding to holding – as the locked load frame and sample relax – then gradually diminishes over time during the hold period. Following shear re-activation, friction coefficient peaks, surpassing the prior steady-state friction coefficient

Table 1
Experimental protocol for slide-hold-slide tests.

Case	*JRC*		Normal stress (MPa)	Shear velocity (μm/s)
1	Average *JRC* = 11.72	*JRC* = 10.85	40	10
2		*JRC* = 11.90	30	10
3		*JRC* = 11.52	20	10
4		*JRC* = 11.78	40	3
5		*JRC* = 12.55	40	1
6	*JRC* = 3.05		40	10
7	*JRC* = 1.49		40	10

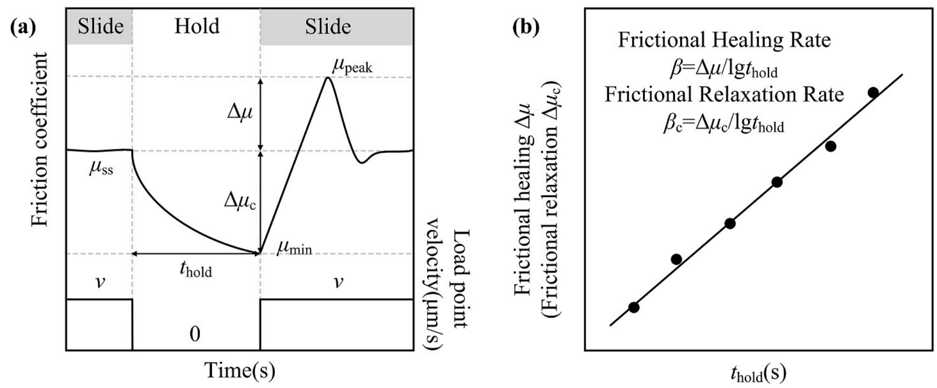

Fig. 2. (a) Schematic of idealized response to the slide-hold-slide (SHS) test, showing the variation of friction coefficient μ and shear velocity v over time. During each hold period (t_{hold}), the friction coefficient decreases ($\Delta\mu_c$) due to specimen creep, before increasing again in subsequent reactivation until reaching a new peak after slip recovery ($\Delta\mu$). (b) Determination of frictional relaxation ($\Delta\mu_c$) and frictional healing ($\Delta\mu$), with the logarithm of hold time (t_{hold}) and determination of frictional healing rate β and frictional relaxation rete β_c.

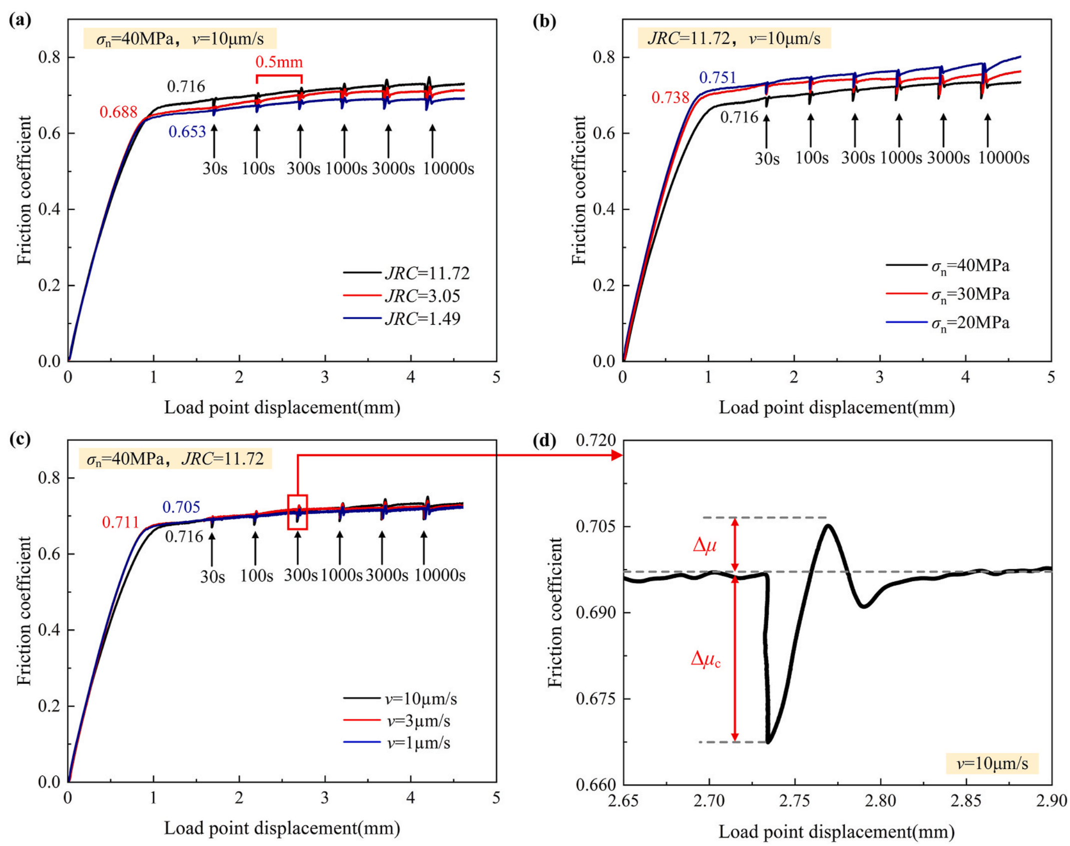

Fig. 3. Typical results of SHS experiments conducted under different combinations of (a) Fracture roughness (*JRC*), (b) Normal stress (σ_n), and (c) Shear velocity (v), defining evolution of friction coefficient with load point displacement. Hold times in each sequence are for 30, 100, 300, 1000, 3000, and 10,000 s. Panel (d) shows a typical result for a shear velocity of 10 μm/s and hold time of 300 s.

before the hold. Subsequently, the friction coefficient stabilizes at a value approximately equivalent to the previous steady-state. This behavior is characteristic of Dieterich-type frictional healing.[18,69]

Frictional healing reflects the shear stress recovery following the stress drop, and frictional relaxation is the result of both the creep of fault materials and the relaxation of the apparatus, both of which are vital in defining earthquake recurrence during interseismic slip.[37,70] To analyze the effects of frictional healing and frictional relaxation under different influencing factors, we use the frictional healing parameter ($\Delta\mu$) and frictional relaxation ($\Delta\mu_c$) to fit the curves of friction versus holding time, as shown in Fig. 5. The results indicate a logarithmic correlation between each of $\Delta\mu$ and $\Delta\mu_c$ with t_{hold} in the range of 30–10000 s, consistent with previous studies.[20,50,71] Both frictional healing $\Delta\mu$ and creep relaxation $\Delta\mu_c$ scale with the logarithm of hold time for all three influencing factors studied (see Fig. 5). Higher frictional healing and creep relaxation values are observed for rougher fractures, faster shearing velocities and longer hold times. In contrast, increased frictional healing and reduced creep relaxation are observed under higher normal stress.

The rates of frictional healing β and relaxation β_c are obtained by least squares fitting of the healing/relaxation-hold time curves with these two parameters importantly associated with earthquake scaling.[70]

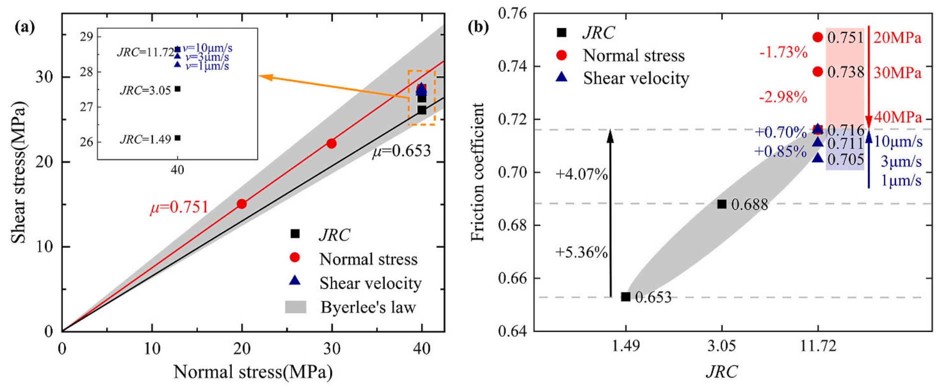

Fig. 4. (a) Friction coefficient measured under the experimental conditions conforms approximately to Byerlee's law. (b) Variation in friction coefficient with fracture roughness, normal stress and shear velocity.

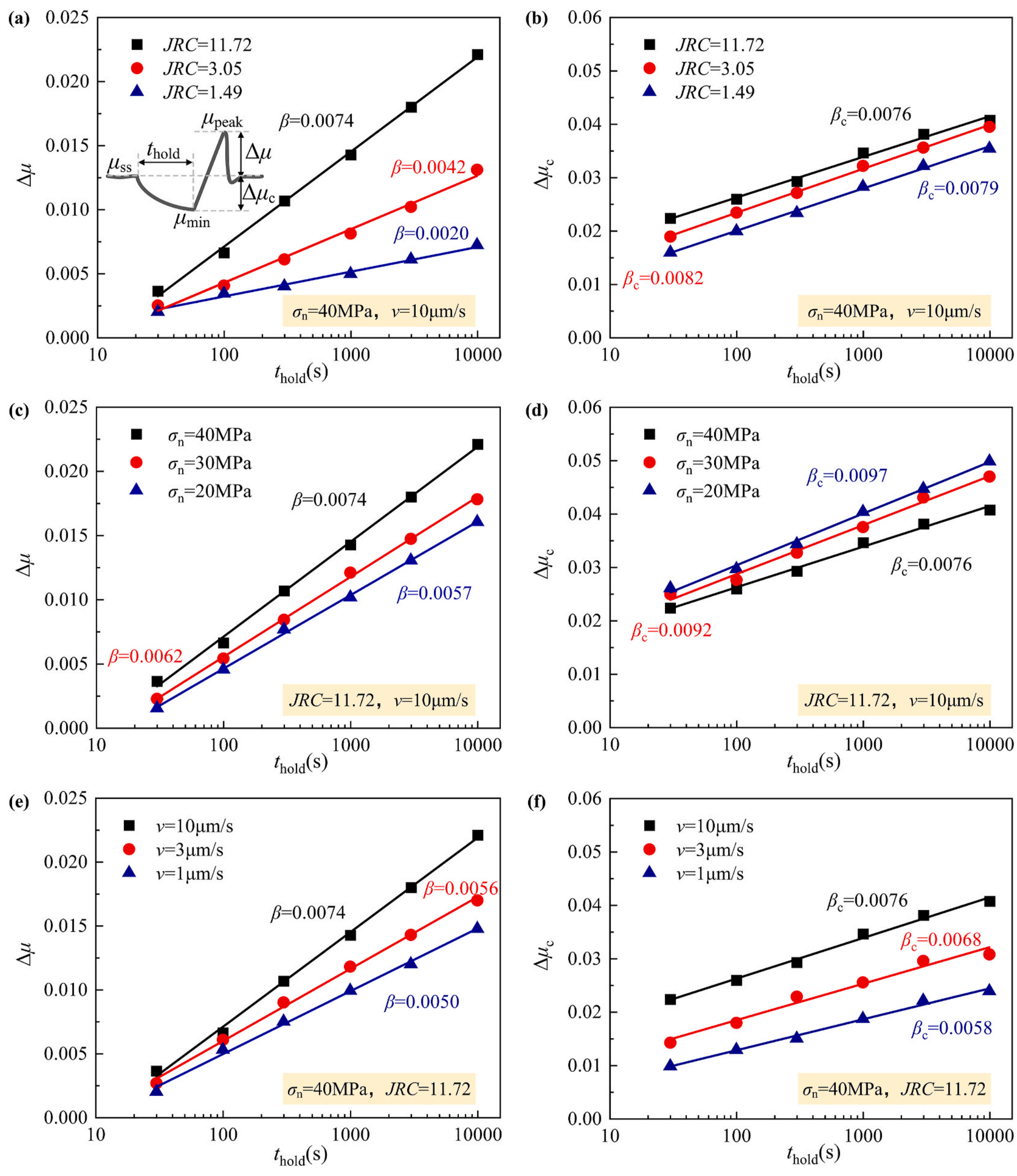

Fig. 5. Frictional healing ($\Delta\mu$) and frictional relaxation ($\Delta\mu_c$) as a function of the logarithm of hold time (t_{hold}) as obtained through SHS tests under different combinations of (a & b) Fracture roughness (*JRC*), (c & d) Normal stress (σ_n), and (e & f) Shearing velocity (v). Inset in panel (a) illustrates ideal outcomes of the SHS tests.

The rate of frictional healing is an essential parameter controlling the features of fault rupture and interseismic stress drop.[24,31] Higher healing rates imply that the frictional strength necessary to prime fault re-rupture is recovered rapidly during the interseismic period, with an important impact on repeated seismic cycles.[72] Meanwhile, earthquake afterslip results from the stress relaxation, and thus, the creep relaxation during a certain hold is associated with earthquake afterslip.[73]

Within our test conditions, β ranged from 0.0020 to 0.0074, and β_c ranged from 0.0058 to 0.0097. For varying fracture surface roughness (*JRC*), β increases with an increase in *JRC*, while β_c diverges slightly without significant difference; for different normal stresses (σ_n), β and β_c are close at 20 MP and 30 MPa but show an obvious increasing trend at 40 MPa whereas β_c decreases; for different shear velocities (v), both β and β_c increase with increments of v.

Within the range of experimental conditions, these results demonstrate significant effects of fracture surface roughness (*JRC*), normal stress (σ_n), and shear velocity(v) on frictional healing. In contrast, their impact on frictional relaxation remains less pronounced.

3.3. Slip weakening

After reaching peak frictional strength upon reloading, we observed a noticeable decrease in frictional force with increasing slip distance, defined as stress drop $\Delta\tau$. This distance is referred to as the slip weakening distance d_w. The evolution of shear stress from peak to a new steady-state value with shear displacement is shown in Fig. 6(a).

Previous studies have reported a logarithmic correlation between d_w and hold time.[74] The data for all samples within the experimental range of $\Delta\tau$ and d_w are depicted in Fig. 6(b)–(d). The results indicate a linear correlation between stress drop $\Delta\tau$ and slip weakening distance d_w, both of which increase with prolonged holding time. Most data show stress drops within the 0.1–1.3 MPa range, corresponding to slip weakening distances of approximately ~0.025 mm. Under similar normal stress and shear velocity conditions, smoother fault surfaces exhibit reduced stress drops and slip-weakening distances. For *JRC* values of 3.05 and 1.49, the maximum stress drops and slip weakening distances are 1.15 MPa, 0.023 mm, and 0.84 MPa, 0.016 mm, respectively. Similarly, at lower normal stress and shear velocities, stress drops and slip-weakening distances decrease. At $\sigma_n = 30$ MPa and $\sigma_n = 20$ MPa, the corresponding maximum stress drops and slip-weakening distances are 0.7 MPa, 0.022 mm, and 0.45 MPa, 0.018 mm, respectively. For shear velocities $v = 3$ μm/s and $v = 1$ μm/s, the maximum stress drops and slip weakening distances are 1.18 MPa, 0.021 mm, and 1.45 MPa, 0.011 mm, respectively.

We also observed that observations for different roughness faults and normal stresses fall on a single trend line, while data under different shearing velocities are more scattered. Thus, within the experimental range, roughness and normal stress tend to elicit variations in stress drop, whereas shearing velocity tends to alter slip-weakening distances.

Additionally, we utilized the stiffness ratio $\kappa = k_s/k_f$ to estimate the stability of fault sliding.[75] If the ratio is less than 1, indicating that the loading system stiffness k_s is less (softer) than that of the fault k_f. In this case, if the experimentally obtained a-$b < 0$, unstable sliding may occur. The loading system stiffness k_s is determined from the series stiffness of the apparatus (load frame) k_m and rock matrix k_r, evaluated as $k_s = 1/(1/k_r + 1/k_m)$. Estimated stiffness for the rock matrix is $k_r = E/L$, where, for the sandstone sample, Young's modulus E obtained from experiments is 14.3 GPa, and the sample length L is 100 mm, for a k_r of 143 MPa/mm. The equipment stiffness k_m is approximately 460~560 MPa/mm, resulting in a range for the loading system stiffness k_s as 109.09–113.91 MPa/mm. Furthermore, we determined the fault stiffness k_f by reloading stiffness, with values ranging from 43–72 MPa/mm.

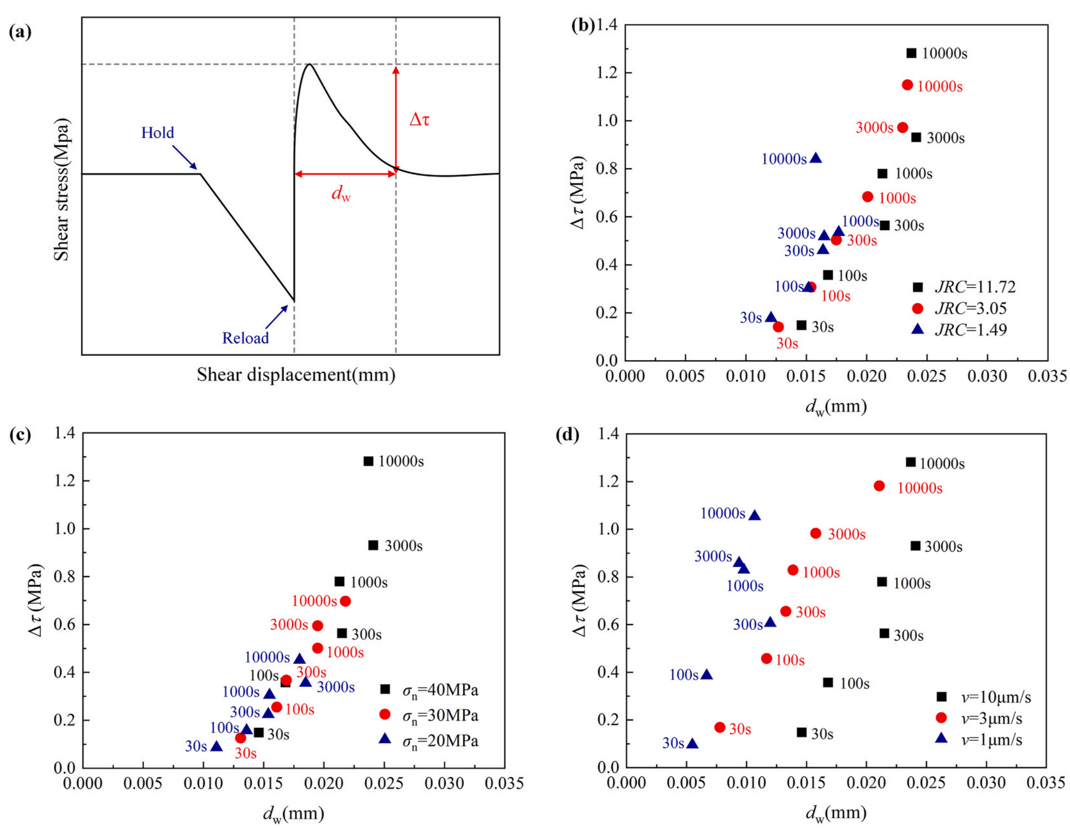

Fig. 6. (a) Schematic representation of SHS test with parameter definitions, showing shear stress as a function of load point displacement. After shear reactivation, the shear stress peaks before asymptotic to a steady magnitude. Stress drop is defined as $\Delta\tau$ and slip weakening distance as d_w. (b) Experiment results of stress drop $\Delta\tau$ and slip weakening distance d_w measured during shear reactivation following hold periods of 30, 100, 300, 1000, 3000, and 10,000 s under different combinations of fracture roughness (*JRC*), (c) Normal stress (σ_n), and (d) Shear velocity (v).

Thus, the stiffness ratio $\kappa = k_s/k_f > 1$, indicating that stable fault sliding is favored despite the slip-weakening response of all samples.

3.4. Mechanistic description of frictional evolution

The frictional strength and healing effects of fractures are closely related to the contact area and contact strength during frictional sliding. Due to the limitations of the experimental setup, direct measurement of changes in contact area is not feasible. To quantify the influence of fracture roughness on frictional strength and sliding behavior, a 3D morphology scanner was employed to map the fracture surfaces before and after shearing. Fig. 7 presents the changes in surface topography and the histograms of asperity heights both before then after shearing for different fracture roughnesses.

As shown in Fig. 7, asperity heights before and after shearing follow a normal distribution, with the mean centered around zero. The rougher the fracture surface, the larger the standard deviation before shearing. Under high normal stress, asperities undergo intense crushing during shearing, with wear debris filling the intervening depressions, leading to a smoother post-shear surface and evidenced by a reduced standard deviation of the normal distribution. Conversely, for smooth surfaces, the changes in surface topography before and after shearing are negligible.

Additionally, the post-shear surface becomes smoother under higher normal stress and for faster shearing velocities and is evident as the standard deviation of the normal distribution reduces over that of the original data (Fig. 8).[76] Moreover, there is a significant difference in pre- and post-shear asperity height at the shearing-front, attributed to plowing of the shearing front and the higher part from the accumulation of wear products.

Fig. 9 illustrates the changes in *JRC* values before and after shearing, as well as the *JRC* reduction ratio. The *JRC* reduction ratio decreases more with increasing normal stress, faster shearing velocities, and rougher fracture surfaces - with normal stress having the most significant influence. These observations are consistent with stronger compaction resulting in greater deformation of asperities, thereby manifesting as a reduced roughness contrast from the shear response.

By integrating the variations in the frictional healing rate during the sliding process with the *JRC* reduction ratio, we can infer that higher normal stress, faster shearing velocities and rougher fractures result in a larger contact area during shearing, thereby inducing increased creep during the hold period.

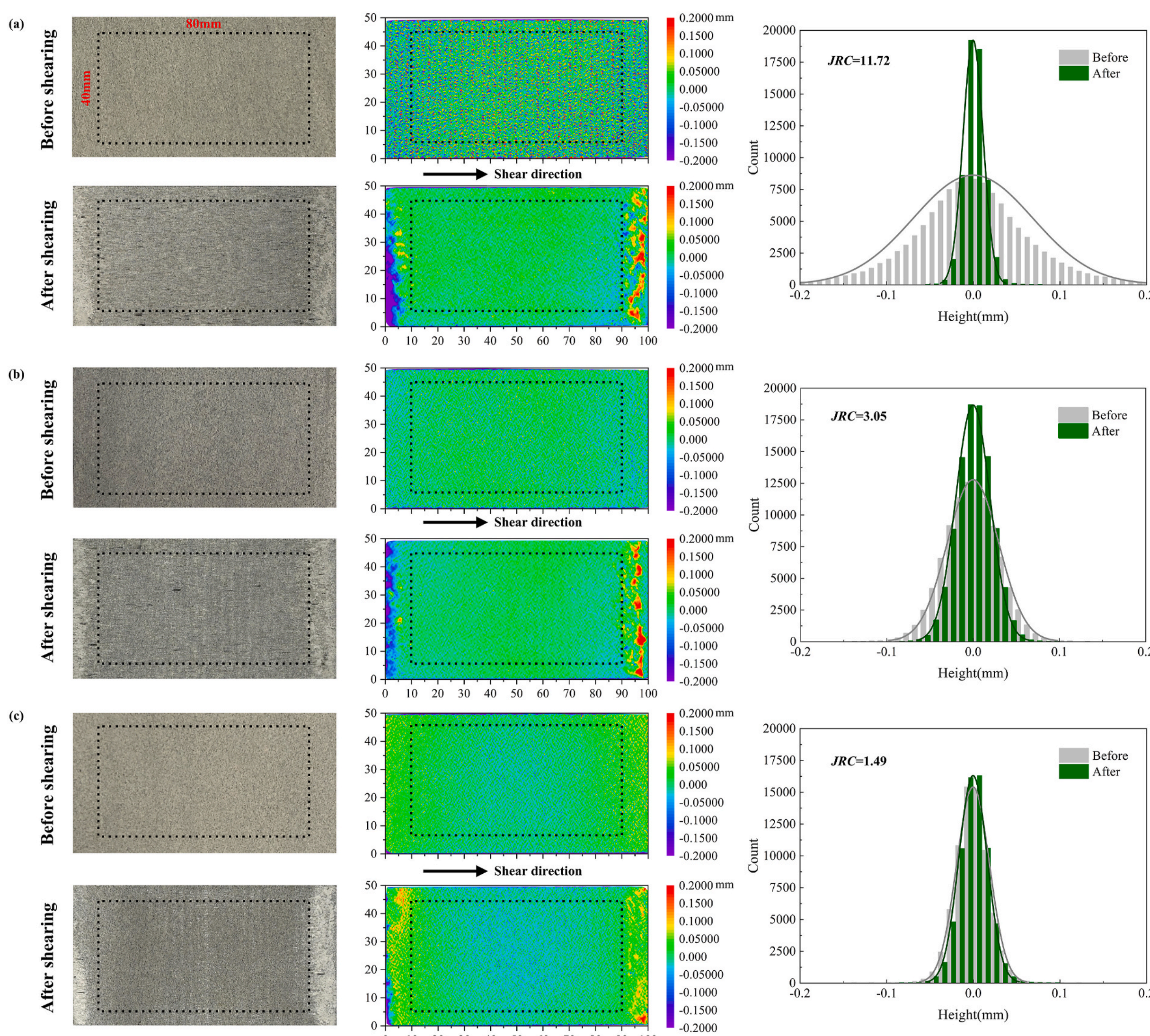

Fig. 7. Optical images of fracture surfaces both before (top left) and after (bottom left) experiments for three different roughness levels: (a) $JRC = 11.72$, (b) $JRC = 3.05$, and (c) $JRC = 1.49$. The research area on the fracture surface is indicated within the black dashed box. Arrows indicate shear direction of the fracture surface. Corresponding surface elevation distribution maps for the asperities are shown in panels to the right.

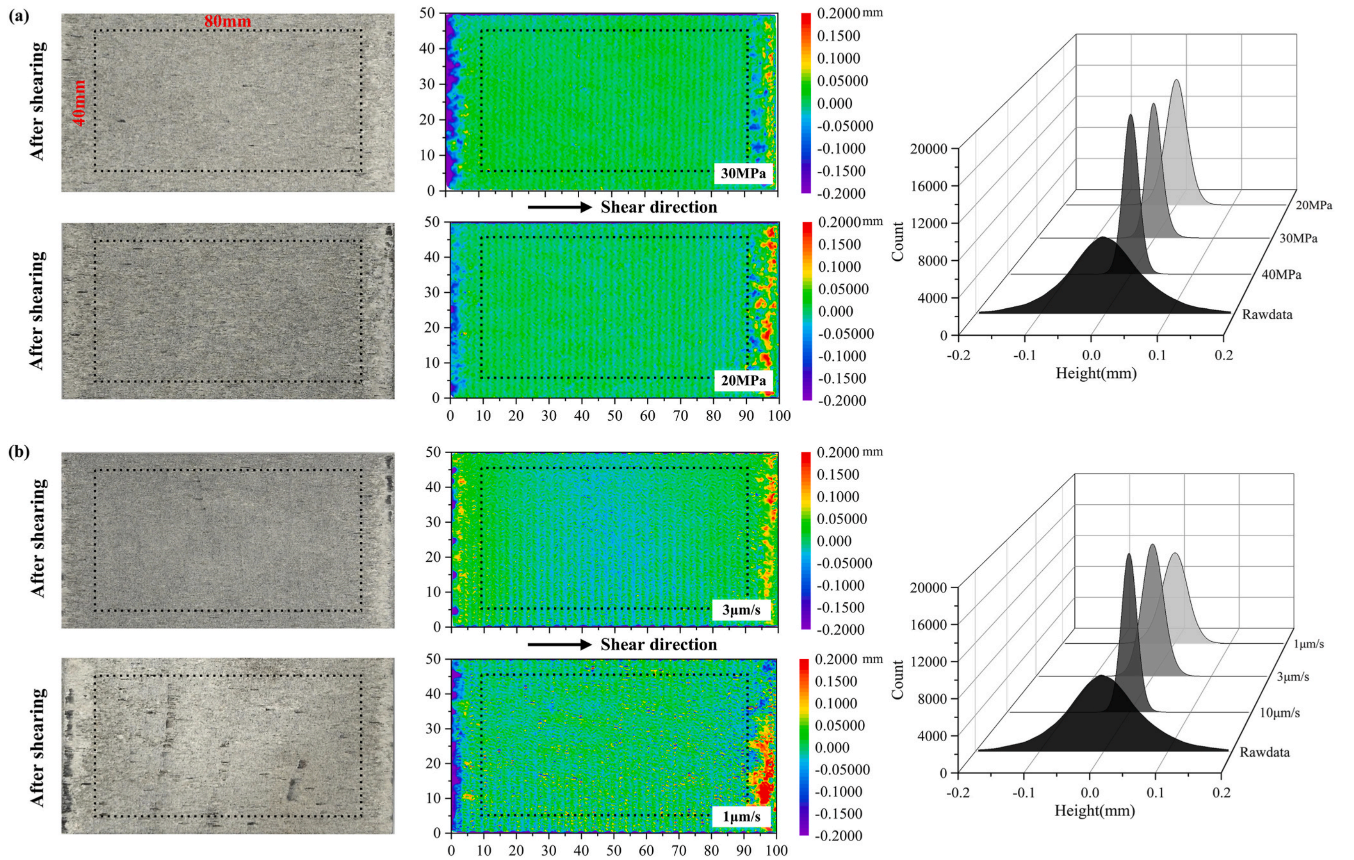

Fig. 8. Surface morphology post-experiment for saw-cut fractures under different conditions of (a) normal stress and (b) shearing velocity. The research area on the fracture surface is indicated within the black dashed box. Arrows indicate the shear direction of the fracture surface. Corresponding surface elevation distribution maps for the asperities are shown in panels to the right.

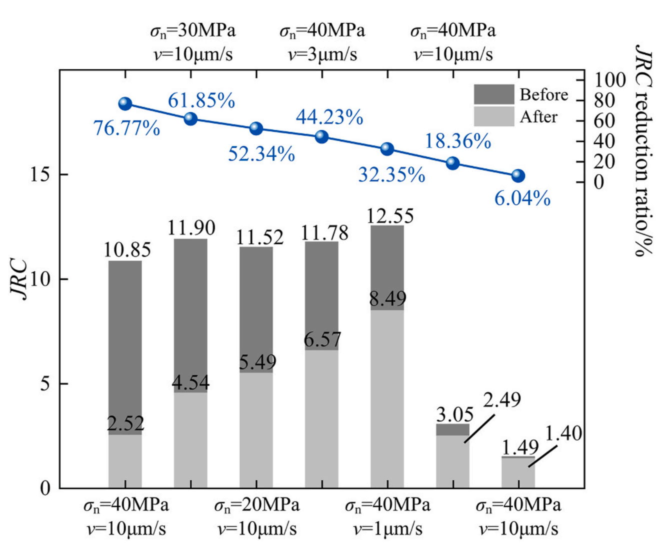

Fig. 9. *JRC* values for the various fracture surfaces pre- and post-experiment, together with change (reduction) in *JRC* due to shearing.

4. Discussion

4.1. Experimental observations

Present observations indicate that the frictional strength of the fractures in sandstone ranges from 0.653 to 0.751. These values are consistent with friction coefficients of sandstone previously obtained at room temperature.[77] Previous observations have extensively shown that the friction coefficient increases with fracture roughness. Additionally, all samples exhibited a trend of decreasing friction coefficient with increasing normal stress and increasing friction coefficient with increasing shearing velocity. Similar dependencies on normal stress and shear velocity have been observed in other samples.[78–80] The phenomenon of friction coefficient decreasing with increasing normal stress and increasing with increasing shear velocity can be explained by the theory of frictional adhesion and the competitive mechanisms between rough surface deformation and microscale asperity sliding.[80] Under conditions of lower normal stress and higher shear velocity, the friction coefficient is primarily influenced by the dilation resulting from asperity contact deformation and the friction angle of the surface. However, as the normal stress increases and shear velocity decreases, the friction mechanism shifts predominantly towards asperity rupture, leading to a reduction in the friction angle and a consequent decrease in frictional strength on the fracture.

Furthermore, we observed that within the range of experimental conditions, the frictional healing rate β of the sandstone samples ranged from 0.0020 to 0.0074, and the frictional relaxation rate β_c ranged from 0.0058 to 0.0097. These results are higher than those obtained from SHS experiments on sandstone fault gouges under similar stress and shear velocity conditions.[32] In the following discussion, we analyze how the observed trends in frictional healing and frictional relaxation effects depend on various factors explored in this work, namely fracture surface roughness, normal stress, and shear velocity.

4.2. Factors influencing frictional healing

During sliding, the asperities on the fracture surface may shear off, wear down, and compact. Over the hold phase, the apparent friction coefficient of the fracture surface gradually decreases with time despite the absence of significant macroscopic sliding. This may be attributed to the creeping deformation of the contacting asperities, including plastic flow of the material around the contact points, the unfolding and closing of microcracks, and the slip of grain boundaries all of which lead to a change in the actual contact area or weakening of local contact points.[75,81,82] At the same time, the hold phase may also lead to compaction of the wear products on the fissure surface, due to the prolonged exposure to normal stresses. This compaction can increase the contact area and contact strength,[83–85] which accumulates the deformation and elastic strain energy required for the next slip and facilitates the frictional healing process. Upon slip re-activation, the bonded particles and asperities need to overcome the contact adhesion so that the friction coefficient is greater than the steady state coefficient formed during the previous shear.

As roughness of the fracture surface increases, the stress concentration between the contact points (or microscopic projections) becomes more pronounced. This stress concentration results in localized stresses exceeding the strength of the rock asperities during arrest, which in turn results in microdamage, plastic deformation, or microcrack extension These localized deformation and damage processes promote the redistribution of stresses across the contact surfaces, which leads to frictional relaxation. The rougher the fracture surface, the more deformation and remolding may occur at the contacting asperities point during arrest. These effects then lead to changes in the contact area, promoting frictional relaxation due to creep and other effects. Although the macroscopic contact area of the rough surface remains constant, the localized increase in roughness results in an increase in the real microscopic contact area.[86] During retention, these contact points may undergo chemical transformation, formation of material bridges, or enhanced mechanical occlusion, thus increasing the degree of frictional healing.

As the normal stress increases, the real contact area between the rock contact surfaces increases. Since more microscopic projections are involved in the shear process, the contact surfaces distribute the stresses more uniformly. Under these conditions, even though plastic flow or creep deformation on the microscopic scale occurs, the stress distribution on individual contact points becomes more uniform due to the increase in the number of contact points. This correspondingly reduces the local stress concentration, leading to a reduction in the frictional relaxation effect. Higher normal stresses promote closer contact between the contacting fracture surfaces and compaction of wear material on the fissure surfaces. This increases mechanical interlocking and possibly chemical bonding, thus increasing frictional strength, an effect that contributes to increased frictional healing.

At higher shear velocities, the adjustment of stress at the contact interface occurs more rapidly, which may result in increased heterogeneity in the stress distribution, thereby promoting frictional relaxation. Under high shearing velocities, the microstructure on the contacting fracture surface may undergo rapid changes, including rupture and recompaction. During high-velocity slip, the temperature increase caused by shear heating may enhance frictional healing by strengthening chemical bonds at the rough contact interface.[87] We quantitatively compared the effect of increasing shear velocity by an order of magnitude on temperature rise using Equation. (4),

$$\theta_w = \frac{\pi \alpha_{th}}{V^2}\left(\frac{\rho c(T_w - T)}{\tau_c}\right)^2 \tag{4}$$

where α_{th} is the thermal diffusivity, c is the heat capacity per unit volume, ρ is the density, τ_c is the shear strength, V is the shear velocity, T is the initial temperature, and T_w is the temperature reached by the rough interface at a given time θ_w. The ratio $(T_{w1}\text{-}T)/(T_{w2}\text{-}T)$ was calculated, and by substituting the parameters under different shear velocity conditions, the ratio was found to be approximately 1.61. This indicates that when the slip velocity increases by an order of magnitude, the temperature on the fracture surface increases by a factor of 1.61. This rapid re-compaction process, together with the elevated temperature, aids in the "healing" of micro-damage on the contact surface, increasing the actual contact area, thereby enhancing frictional healing. In contrast, the temperature increase due to shear heating is minimal under low-velocity slip.

4.3. Characteristics of acoustic emission

Rock is a typical brittle material, and when asperities on rough surfaces are sheared off or worn down during the shear process, they release elastic strain energy in the form of elastic waves, recorded as acoustic emission (AE) signals. Each AE signal released during the shear process corresponds to a damage or fracture event. Therefore, mechanisms of shear failure may be recovered by analyzing the AE signals during shearing.

Fig. 10 (a) and (b) respectively present the evolution curves of the AE ring-down counts and cumulative ring-down counts at a shear rate of 1 μm/s (Case5), as well as time-binned AE energy and cumulative AE energy throughout the entire process of frictional sliding. During the slow increase phase in the friction coefficient, AE ring-down counts are relatively low. Thus, the energy generated by AE is minimal, leading to a slow increase in both cumulative ring-down counts and cumulative AE energy. In this phase, only minimal damage occurs on the asperity surfaces, with some asperities being abraded and sheared, emitting AE signals and releasing energy. During the linear growth phase of the friction coefficient, the AE ring-down counts and energy increase significantly, showing natural variability in time. Under peak shear stress conditions, the inferred extent of damage and failure, as well as the damage occurring on the asperities of the rough surfaces, increases markedly. This severe abrasion and shearing of asperities result in maximum AE ring-down counts and energy. Fig. 10 (e) and (f) respectively present the variation curves of the AE ring-down counts and cumulative ring-down counts for Case 1 and Case 3, revealing trends identical to those observed in Case 5. As shown in Fig. 10 (c), during the hold phase of the SHS test, only a few AE ring-down counts and little AE energy are detected, and the growth of cumulative ring-down counts and AE energy is very slow. This stage likely involves damage recovery and crack closure. However, during the sliding re-activation phase, the AE ring-down count and AE energy surge along with the sudden drop in the friction coefficient post-peak, possibly due to the disruption of damage recovery during the hold phase. Interestingly, the AE ring-down count and AE energy generated during each sudden drop in the friction coefficient increase with longer hold times, indicating that prolonged hold periods lead to more significant damage recovery.

Next, the relationship between sliding displacement and cumulative AE energy is explored (Fig. 10 (d)) From the magnified inset in Fig. 10 (d), it can be observed that during the slow increase in shear stress, the interface is in a static frictional state, with an average sliding displacement near zero and a low cumulative AE energy value. In the early stage of linear shear stress increase, the interface transitions between static friction and stable sliding, with nearly linear growth in both average shear displacement and cumulative AE energy. During the sliding phase of the SHS test, the cumulative AE energy and sliding displacement exhibit similar trends; cumulative AE energy increases during sliding, but shows no significant change during the hold phase (excluding noise effects).

From the analysis of the relationship between shear displacement and cumulative AE energy, a strong correlation exists between the evolution of shear displacement and cumulative AE energy. This suggests that cumulative AE energy can be used to qualitatively assess the trend of frictional sliding displacement on rock interfaces.

To directly obtain the seismic moment M_0 for re-activation in the SHS experiments, we absolutely calibrated the AE sensors. We conducted ball drop tests, correlating the seismic moment M_0 induced by internal seismic sources (such as earthquakes and acoustic emissions)

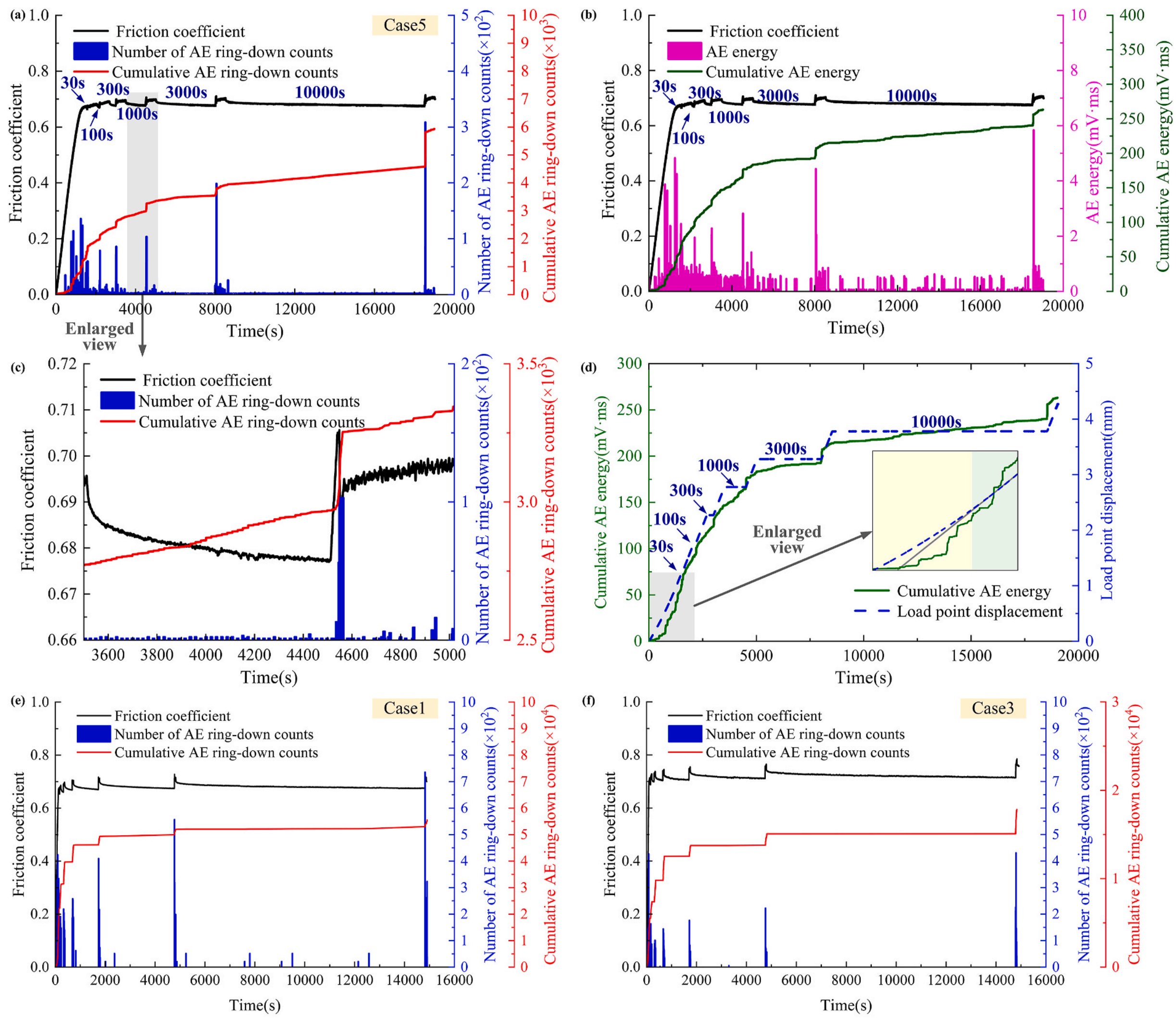

Fig. 10. (a) Evolution of AE ring-down counts and cumulative ring-down counts during frictional sliding for Case 5. (b) Evolution of AE energy and cumulative AE energy during frictional sliding for Case 5. (c) Enlarged view of the gray-shaded region in (a), shows a small number of AE counts during the hold phase, with a sharp increase as the coefficient of friction drops suddenly during slip reactivation during the slip phase, followed by fluctuating changes post-peak. (d) Cumulative AE energy with sliding displacement. (e) Evolution of AE ring-down counts and cumulative ring-down counts during frictional sliding for Case 1. (f) Evolution of AE ring-down counts and cumulative ring-down counts during frictional sliding for Case 3.

with the impulse or momentum change Δp of an externally applied seismic source (ball impact).[88] This method utilizes a small ball that impacts the sample surface as a reference source, thereby linking the absolute amplitude of seismic waves to the momentum of the decelerating ball. The momentum of the ball can be directly measured or readily estimated based on its mass and drop height.

In the ball drop experiment (as shown in Fig. 11(a)), the sample was placed on a platen made from the same material and of the same height as in the experimental setup. Two AE sensors positioned on the platens recorded the acoustic emission conditions during the SHS tests. Calibration was with a 5.16g glass ball free-falling from a height of 34 cm, with its momentum Δp estimated to be 0.0172 J (based on mass and drop height). The surface of the sample was marked with a lattice of five points (P1–P5), with 10 ball drop tests performed at each point. The amplitude data of the acoustic emissions recorded showed minimal variation (as shown in Fig. 11(b)), with an average amplitude A from 50 tests of 159.85 mV in recorded units. The relationship between amplitude A and momentum Δp is constant with the ratio, k, given by $k = \Delta p / A = 1.076 \times 10^{-4}$.

Using this absolute calibration, we can approximate the cumulative seismic moment corresponding to the AE amplitude generated during each sliding event in the SHS test. The specific results are presented in Table 2. Extensive seismic observations indicate a relationship between the cumulative seismic moment ΣM_0 and the slip area, as follows:

$$\Sigma \boldsymbol{M}_0 = \boldsymbol{G A} \Delta \boldsymbol{u} \tag{5}$$

where ΣM_0 represents the cumulative seismic moment, G is the shear modulus, A is the slip area, and Δu is the slip distance, fixed at 0.5 mm. The shear modulus G is determined by the product of the shear stiffness and the thickness perpendicular to the shear plane (50 mm), with the shear stiffness calibrated based on the elastic stiffness of the fault before the peak (as shown in Fig. 11(c)).

The slip area for each sliding event was calculated using Equation. (5) (as shown in Fig. 11(d)). The slip area increases logarithmically with the hold time, further validating the time-dependent nature of friction healing.

4.4. *Fitting experimental data and inversion for RSF frictional parameters*

To validate whether the experimental data can be accurately modeled using RSF, we employed RSFit3000[89] to fit the SHS experiments. We

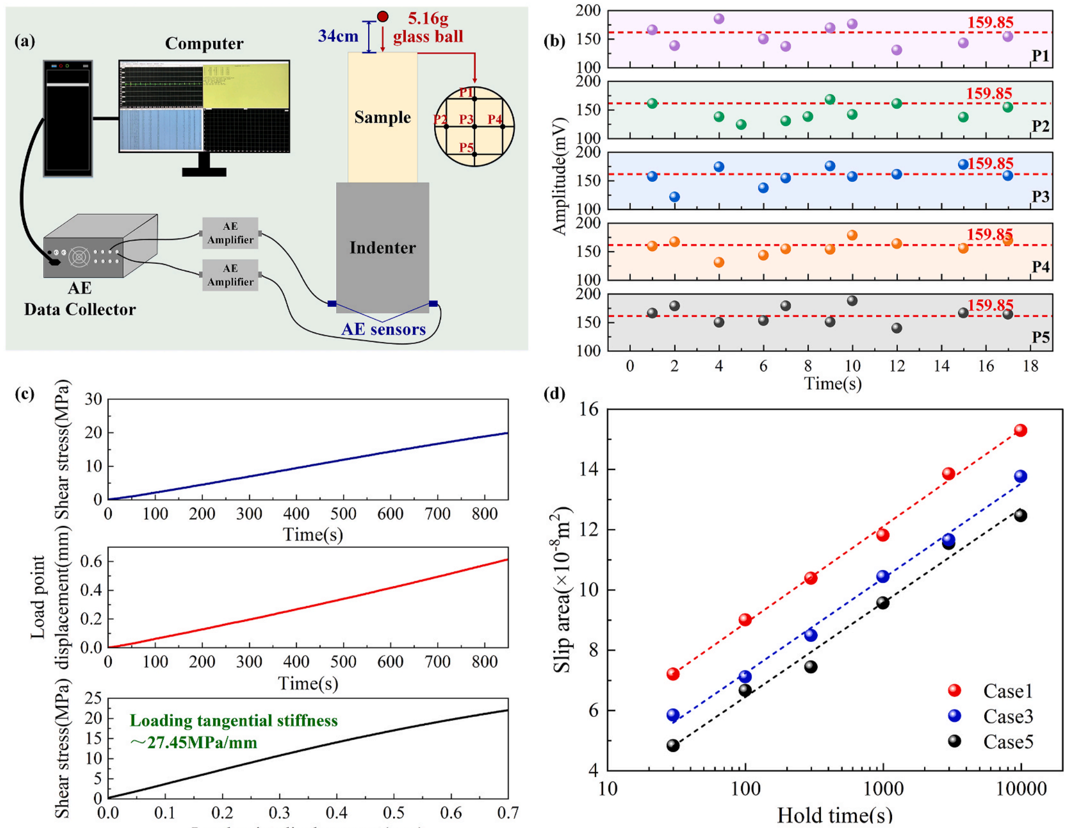

Fig. 11. (a) Schematic of ball drop experimental setup with AE sensors attached to the indenter surface. Inset illustrates the target of five marked points for successive ball-drops (P1-P5). (b) AE amplitudes from 50 ball drops. (c) Shear stress versus loading time (top), load point displacement versus loading time (middle), and shear stress versus load-point displacement curves (bottom) during initial shear stress loading. (d) Variation in slip area with logarithm of hold time.

Table 2
Cumulative AE amplitudes, cumulative seismic moment and slip areas at various hold times.

Case NO.	Hold time (s)	Cumulative AE amplitude (mV)	Cumulative seismic moment (N·m)	Slip area ($\times 10^{-8}$m^2)
Case1	30	459.25	0.0494153	7.200772313
	100	574.25	0.0617893	9.003905282
	300	662.33	0.0712667	10.38494834
	1000	753.58	0.0810852	11.81569515
	3000	883.61	0.0950764	13.85448976
	10000	975.33	0.1049455	15.2926059
Case3	30	372.48	0.0400789	5.84026929
	100	453.62	0.0488095	7.112497195
	300	541.23	0.0582363	8.486170929
	1000	665.85	0.0716452	10.44013989
	3000	743.92	0.0800458	11.66423199
	10000	878.23	0.0944975	13.7701345
Case5	30	288.11	0.0310008	4.51664
	100	397.66	0.0427884	6.23403
	300	444.07	0.0477822	6.96159
	1000	571.09	0.0614496	8.95286
	3000	689.19	0.0741572	10.8043
	10000	744.43	0.0801011	11.6703

inverted the data to obtain the best-fitting constitutive parameters a, b, and D_c by applying an iterative least-squares method. The aging law was selected to simulate the evolution of the state variable.

The state variable was computed using the highly accurate ode45 solver, a built-in MATLAB function based on the 4th-order Runge-Kutta method, with adaptive time-stepping. The detailed solution process is presented in Equation. (6):

$$\begin{cases} \boldsymbol{K}_1 = 1 - \dfrac{\boldsymbol{v}_{t+\Delta t}\boldsymbol{\theta}_t}{\boldsymbol{D}_c} \\ \boldsymbol{K}_2 = 1 - \dfrac{\boldsymbol{v}_{t+\Delta t}}{\boldsymbol{D}_c}\left(\boldsymbol{\theta}_t + \dfrac{\Delta t}{2}\boldsymbol{K}_1\right) \\ \boldsymbol{K}_3 = 1 - \dfrac{\boldsymbol{v}_{t+\Delta t}}{\boldsymbol{D}_c}\left(\boldsymbol{\theta}_t + \dfrac{\Delta t}{2}\boldsymbol{K}_2\right) \\ \boldsymbol{K}_4 = 1 - \dfrac{\boldsymbol{v}_{t+\Delta t}}{\boldsymbol{D}_c}\left(\boldsymbol{\theta}_t + \Delta t\boldsymbol{K}_3\right) \\ \boldsymbol{\theta}_{t+\Delta t} = \boldsymbol{\theta}_t + \dfrac{\Delta t}{6}\left(\boldsymbol{K}_1 + 2\boldsymbol{K}_2 + 2\boldsymbol{K}_3 + \boldsymbol{K}_4\right) \end{cases} \tag{6}$$

In Equation. (6), θ_t represents the state variable at time t, and K_i (i = 1–4) are intermediate variables. Fig. 12(a)–(g) show the specific fitting results, presenting only the cases with a hold time of 30 s. From the figures, it is evident that the experimental data closely align with the simulated results, confirming that the experimental results can be effectively modeled using RSF.

Additionally, the simulated values of direct, a, and evolutionary, b, effects were compared with the experimentally obtained values of frictional relaxation $\Delta\mu_c$ and frictional healing $\Delta\mu$, respectively, under the influence of three different factors, as shown in Fig. 12(h) and (i). The figures indicate that the trends in a and b correspond closely with those of $\Delta\mu_c$ and $\Delta\mu$, suggesting a strong physical relationship between these two frictional characteristics and the direct and evolutionary state effects described in the RSF model. This is consistent with the findings of previous studies.[90]

During the interseismic period, the fault slip rate is relatively low, allowing the fault to undergo compaction through creep, thereby enhancing its strength. This process governs stress accumulation during

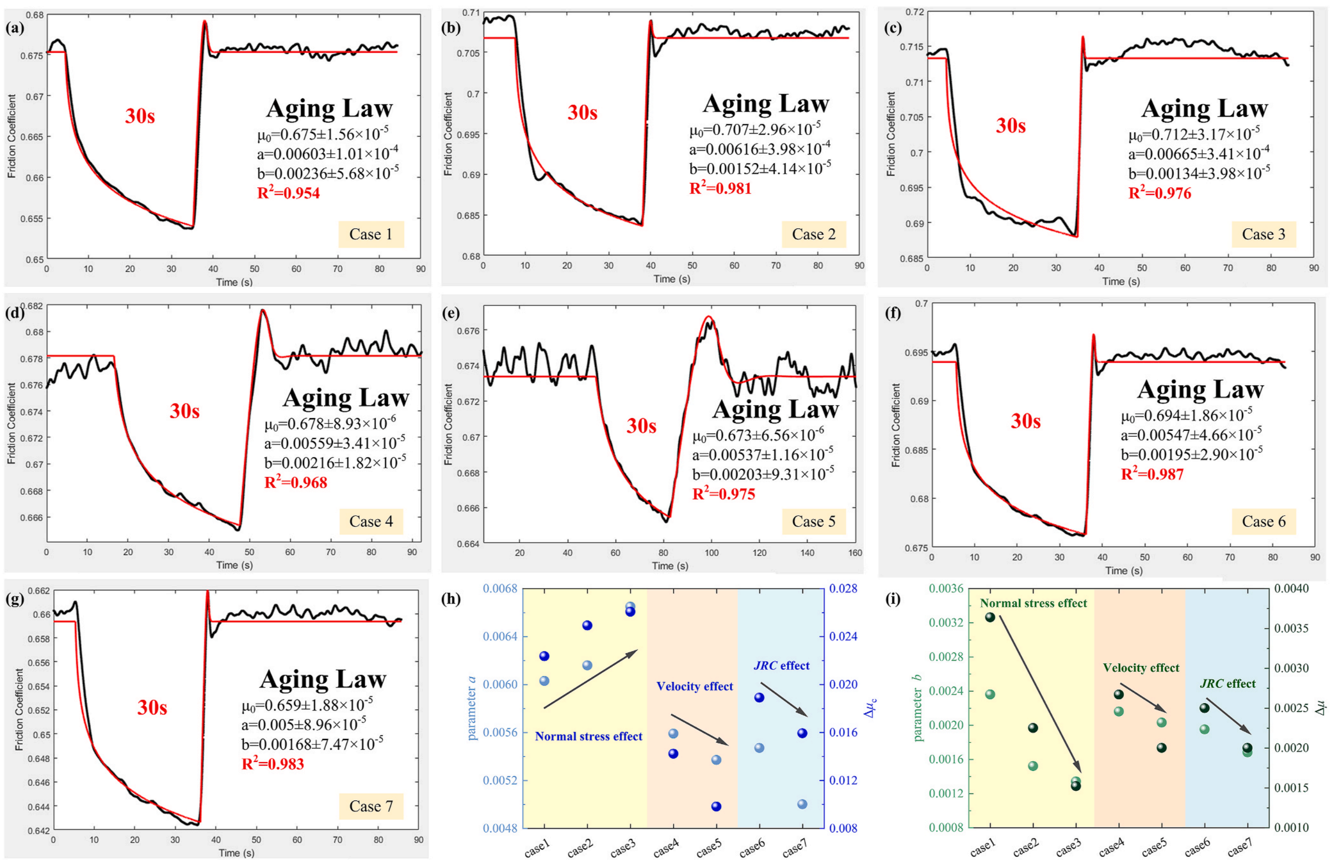

Fig. 12. (a)–(g) Fitted friction coefficients using RSFit3000 for hold times of 30 s in each case. Simulated values of (h) RSF-*a* and (i) RSF-*b* parameters are compared with the experimentally obtained frictional relaxation magnitudes $\Delta\mu_c$ and healing magnitudes $\Delta\mu$, respectively, as they vary with the three influencing factors.

the interseismic period and determines when sufficient stress has built to exceed strength and to trigger the next seismic event. The longer the interseismic period, the greater the energy accumulated by the fault. When the fault experiences seismic slip, the frictional force rapidly recovers, exhibiting healing behavior. The magnitude of frictional healing immediately prior to an earthquake controls the resistance during fault slip and the rate of energy release. A larger *b* value indicates stronger frictional recovery during slip, leading to a more rapid and intense energy release, which may result in a larger event.

5. Conclusions

We conducted SHS experiments on fractures in sandstone at room temperature to investigate the frictional strength, post-slip strength recovery, reactivation, and subsequent sliding behavior of these materials. The effects of roughness (JRC = 11.72, 3.05, 1.49), normal stress (σ_n = 20, 30, 40 MPa), and shear velocity (v = 1, 3, 10 μm/s) on frictional strength and time dependence were examined, with the hold times ranging from 30s to 10000s. Data fitting was performed using RSF via matching in time with a fourth-order Runge-Kutta method.

Our observations revealed that the frictional strength (μ = 0.653–0.751) of the fractures was primarily influenced by the surface roughness, followed by normal stress, with the shearing velocity having the least impact. Friction coefficient increased with surface roughness and shearing velocity but decreased as normal stress increased. Frictional healing was found to be significantly dependent on surface roughness, normal stress, and shear velocity. Under the same hold time, increases in surface roughness, normal stress and shear velocity accelerated friction healing, while higher normal stress inhibited friction relaxation.

Evolution of the contact area was the main contributor to frictional healing on the exposed surface. By comparing fracture surface morphology between pre- and post-shear and quantitatively analyzing changes in damaged asperities, the change in contact area depended on fracture surface roughness, normal stress and shear velocity. The *JRC* reduction ratio was greater with increasing normal stress, shear velocity and fracture surface roughness, which also corresponded to the changes in friction healing.

Real-time AE monitoring was also conducted during the experiments. It was observed that during the sliding phase, AE ring-down counts and energy increased sharply with the sudden drop in shear stress, fluctuating after reaching a peak. As the hold time increased, the AE ring-down counts and energy generated by each shear stress drop also increased. Measuring actual seismic moments using absolutely calibrated AE sensors allowed changes in microscopic contact area to be inferred from prescribed seismic moments - quantitatively determining the change in contact area during the slip cycle. Contact area was shown to evolve with the logarithm of hold time, corroborated with the time-dependent evolution of healing obtained from the SHS experiments.

CRediT authorship contribution statement

Quan Gan: Writing – review & editing, Supervision, Resources, Funding acquisition, Conceptualization. **Xinyuan Zhang:** Writing – original draft, Visualization, Validation, Investigation, Formal analysis, Data curation. **Qiang Li:** Supervision. **Jianye Chen:** Supervision, Methodology. **Fengshou Zhang:** Supervision. **Zhen Zhong:** Supervision. **Yunzhong Jia:** Supervision. **Pengliang Yu:** Supervision. **Mengke An:** Supervision. **Derek Elsworth:** Writing – review & editing, Supervision.

Declaration of competing interest

The authors declare that they have no known competing financial interests or personal relationships that could have appeared to influence the work reported in this paper.

Acknowledgments

This study was supported by the Joint Funds of the National Natural Science Foundation of China (Grant: U23B20160), General Program of the National Natural Science Foundation of China (Grant: No. 5217041034), CO_2 Enhanced Shale Gas Recovery and Sequestration by Numerical Thermal-Hydro-Mechanical-Chemical Modelling (Grant: 2023DQ02-0206).

Data availability

Data will be made available on request.

References

1. Noël C, Giorgetti C, Scuderi MM, Collettini C, Marone C. The effect of shear displacement and wear on fault stability: laboratory constraints. *JGR*. 2023;128(4). https://doi.org/10.1029/2022JB026191.
2. Morad D, Sagy A, Tal Y, Hatzor YH. Fault roughness controls sliding instability. *Earth Planet Sci Lett*. 2022;579, 117365. https://doi.org/10.1016/j.epsl.2022.117365.
3. Scholz CH, Engelder JT. The role of asperity indentation and ploughing in rock friction - I. Asperity creep and stick-slip. *Int J Rock Mech Min Sci*. 1976;13(5): 149–154. https://doi.org/10.1016/0148-9062(76)90819-6.
4. Xing T, Zhu W, French M, Belzer B. Stabilizing effect of high pore fluid pressure on slip behaviors of gouge-bearing faults. *JGR*. 2019;124(9):9526–9545. https://doi.org/10.1029/2019JB018002.
5. Rouet-Leduc B, Hulbert C, Bolton DC, et al. Estimating Fault friction from seismic signals in the laboratory. *Geophys Res Lett*. 2018;45(3):1321–1329. https://doi.org/10.1002/2017GL076708.
6. Yamashita F, Fukuyama E, Mizoguchi K, Takizawa S, Xu S, Kawakata H. Scale dependence of rock friction at high work rate. *Nature*. 2015;528(7581):254–257. https://doi.org/10.1038/nature16138.
7. Manighetti I, Campillo M, Bouley S, Cotton F. Earthquake scaling, fault segmentation, and structural maturity. *Earth Planet Sci Lett*. 2007;253(3-4):429–438. https://doi.org/10.1016/j.epsl.2006.11.004.
8. Violay M, Giorgetti C, Cornelio C, et al. HighSTEPS: a high strain temperature pressure and speed apparatus to study earthquake mechanics. *Rock Mech Rock Eng*. 2021;54(4):2039–2052. https://doi.org/10.1007/s00603-021-02362-w.
9. Viesca RC. Frictional state evolution laws and the non-linear nucleation of dynamic shear rupture. *J Mech Phys Solid*. 2023;173, 105221. https://doi.org/10.1016/j.jmps.2023.105221.
10. Ellsworth WL. Injection-induced earthquakes. *Science*. 2013;341(6142), 1225942. https://doi.org/10.1126/science.1225942.
11. Shapiro SA, Dinske C, Rothert E. Hydraulic-fracturing controlled dynamics of microseismic clouds. *Geophys Res Lett*. 2006;33(14). https://doi.org/10.1029/2006GL026365.
12. Guglielmi Y, Cappa F, Avouac J, Henry P, Elsworth D. Seismicity triggered by fluid injection–induced aseismic slip. *Science*. 2015;348(6240):1224–1226. https://doi.org/10.1126/science.aab0476.
13. Walsh FR, Zoback MD. Oklahoma's recent earthquakes and saltwater disposal. *Sci Adv*. 2015;1(5), e1500195. https://doi.org/10.1126/sciadv.1500195.
14. Majer EL, Baria R, Stark M, et al. Induced seismicity associated with enhanced geothermal systems. *Geothermics*. 2007;36(3):185–222. https://doi.org/10.1016/j.geothermics.2007.03.003.
15. Bao X, Eaton DW. Fault activation by hydraulic fracturing in western Canada. *Science*. 2016;354(6318):1406–1409. https://doi.org/10.1126/science.aag2583.
16. Elsworth D, Spiers CJ, Niemeijer AR. Understanding induced seismicity. *Science*. 2016;354(6318):1380–1381. https://doi.org/10.1126/science.aal2584.
17. Dieterich JH. Time-dependent friction as a possible mechanism for aftershocks. *JGR*. 1972;77(20):3771–3781. https://doi.org/10.1029/JB077i020p03771.
18. Dieterich JH. Time-dependent friction in rocks. *JGR*. 1972;77(20):3690–3697. https://doi.org/10.1029/JB077i020p03690.
19. Dieterich JH. Time-dependent friction and the mechanics of stick-slip. *Pure Appl Geophys*. 1978;116(4-5):790–806. https://doi.org/10.1007/BF00876539.
20. Marone C. The effect of loading rate on static friction and the rate of fault healing during the earthquake cycle. *Nature*. 1998;391(6662):69–72. https://doi.org/10.1038/34157.
21. Brace WF. Laboratory studies of stick-slip and their application to earthquakes. *Tectonophysics*. 1972;14(3-4):189–200. https://doi.org/10.1016/0040-1951(72)90068-6.
22. Brace WF, Byerlee JD. Stick-slip as a mechanism for earthquakes. *Science*. 1966;153(3739):990–992. https://doi.org/10.1126/science.153.3739.990.
23. Marone C, Vidale JE, Ellsworth WL. Fault healing inferred from time dependent variations in source properties of repeating earthquakes. *Geophys Res Lett*. 1995;22(22):3095–3098. https://doi.org/10.1029/95GL03076.
24. Scholz CH, Aviles CA, Wesnousky SG. Scaling differences between large interplate and intraplate earthquakes. *Bull Seismol Soc Am*. 1986;76(1):65–70.
25. Marone C. On the rate of frictional healing and the constitutive law for time- and slip-dependent friction. *Int J Rock Mech Min Sci*. 1997;34(3-4):181–187. https://doi.org/10.1016/S1365-1609(97)00054-3.
26. Niemeijer AR, Spiers CJ, Peach CJ. Frictional behaviour of simulated quartz fault gouges under hydrothermal conditions: results from ultra-high strain rotary shear experiments. *Tectonophysics*. 2008;460(1-4):288–303. https://doi.org/10.1016/j.tecto.2008.09.003.
27. Beeler NM, Hickman SH, Wong TF. Earthquake stress drop and laboratory-inferred interseismic strength recovery. *JGR*. 2001;106(B12):30701–30713. https://doi.org/10.1029/2000JB900242.
28. Peng Z, Vidale JE, Marone C, Rubin A. Systematic variations in recurrence interval and moment of repeating aftershocks. *Geophys Res Lett*. 2005;32(15), L15301. https://doi.org/10.1029/2005GL022626.
29. Hong T, Marone C. *Effects of normal stress perturbations on the frictional properties of simulated faults. G3*. 2005;6(3), Q03012. https://doi.org/10.1029/2004GC000821.
30. Marone C. Laboratory-derived friction laws and their application to seismic faulting. *Annu Rev Earth Planet Sci*. 1998;26(1):643–696. https://doi.org/10.1146/annurev.earth.26.1.643.
31. Perrin G, Rice JR, Zheng G. Self-healing slip pulse on a frictional surface. *J Mech Phys Solid*. 1995;43(9):1461–1495. https://doi.org/10.1016/0022-5096(95)00036-I.
32. Zhang F, An M, Zhang L, Fang Y, Elsworth D. The role of mineral composition on the frictional and stability properties of powdered reservoir rocks. *JGR*. 2019;124(2): 1480–1497. https://doi.org/10.1029/2018JB016174.
33. Seyler CE, Shreedharan S, Saffer DM, Marone C. The role of clay in limiting frictional healing in fault gouges. *Geophys Res Lett*. 2023;50(20). https://doi.org/10.1029/2023GL104984.
34. Carpenter BM, Ikari MJ, Marone C. Laboratory observations of time-dependent frictional strengthening and stress relaxation in natural and synthetic fault gouges. *JGR*. 2016;121(2):1183–1201. https://doi.org/10.1002/2015JB012136.
35. van den Ende MPA, Niemeijer AR. An investigation into the role of time-dependent cohesion in interseismic fault restrengthening. *Sci Rep*. 2019;9(1):9894. https://doi.org/10.1038/s41598-019-46241-5.
36. Jeppson T, Lockner D, Beeler N, Hickman S. Strength recovery in quartzite is controlled by changes in friction in experiments at hydrothermal conditions up to 200°C. *JGR*. 2023;128(5). https://doi.org/10.1029/2022JB025663.
37. Carpenter BM, Collettini C, Viti C, Cavallo A. The influence of normal stress and sliding velocity on the frictional behaviour of calcite at room temperature: insights from laboratory experiments and microstructural observations. *Geophys J Int*. 2016;205(1):548–561. https://doi.org/10.1093/gji/ggw038.
38. Karner SL, Marone C, Evans B. Laboratory study of fault healing and lithification in simulated fault gouge under hydrothermal conditions. *Tectonophysics*. 1997;277(1-3):41–55. https://doi.org/10.1016/S0040-1951(97)00077-2.
39. Chester FM, Higgs NG. Multimechanism friction constitutive model for ultrafine quartz gouge at hypocentral conditions. *JGR*. 1992;97(B2):1859–1870. https://doi.org/10.1029/91JB02349.
40. Mitchell EK, Fialko Y, Brown KM. *Temperature dependence of frictional healing of Westerly granite: Experimental observations and numerical simulations. G3*. 2013;14(3): 567–582. https://doi.org/10.1029/2012GC004241.
41. Zhong Z, Xu C, Hu Y, Zhang F, Wu F, Li B. Frictional strength and sliding behaviors of an analogue rock-fault structure: a laboratory study. *Int J Rock Mech Min Sci*. 2024;174, 105665. https://doi.org/10.1016/j.ijrmms.2024.105665.
42. Frye KM, Marone C. Effect of humidity on granular friction at room temperature. *JGR*. 2002;107(B11):11. https://doi.org/10.1029/2001JB000654.
43. Byerlee J. Friction of rocks. *Pure Appl Geophys*. 1978;116(4-5):615–626. https://doi.org/10.1007/BF00876528.
44. Shimamoto T, Logan JM. Effects of simulated fault gouge on the sliding behavior of Tennessee Sandstone: nonclay gouges. *JGR*. 1981;86(B4):2902–2914. https://doi.org/10.1029/JB086iB04p02902.
45. Brown KM, Kopf A, Underwood MB, Weinberger JL. Compositional and fluid pressure controls on the state of stress on the Nankai subduction thrust: a weak plate boundary. *Earth Planet Sci Lett*. 2003;214(3-4):589–603. https://doi.org/10.1016/S0012-821X(03)00388-1.
46. Saffer DM, Marone C. Comparison of smectite- and illite-rich gouge frictional properties: application to the updip limit of the seismogenic zone along subduction megathrusts. *Earth Planet Sci Lett*. 2003;215(1-2):219–235. https://doi.org/10.1016/S0012-821X(03)00424-2.
47. Carpenter BM, Saffer DM, Marone C. Frictional properties of the active San Andreas Fault at SAFOD: implications for fault strength and slip behavior. *JGR*. 2015;120(7): 5273–5289. https://doi.org/10.1002/2015JB011963.
48. Ikari MJ, Niemeijer AR, Marone C. The role of fault zone fabric and lithification state on frictional strength, constitutive behavior, and deformation microstructure. *JGR*. 2011;116(B8). https://doi.org/10.1029/2011JB008264.
49. Ruggieri R, Scuderi MM, Trippetta F, et al. The role of shale content and pore-water saturation on frictional properties of simulated carbonate faults. *Tectonophysics*. 2021;807, 228811. https://doi.org/10.1016/j.tecto.2021.228811.
50. Tesei T, Collettini C, Carpenter BM, Viti C, Marone C. Frictional strength and healing behavior of phyllosilicate-rich faults. *JGR*. 2012;117(B9). https://doi.org/10.1029/2012JB009204.
51. Tesei T, Collettini C, Barchi MR, Carpenter BM, Di Stefano G. Heterogeneous strength and fault zone complexity of carbonate-bearing thrusts with possible

implications for seismicity. *Earth Planet Sci Lett*. 2014;408:307–318. https://doi.org/10.1016/j.epsl.2014.10.021.
52. Dewers T, Hajash A. Rate laws for water-assisted compaction and stress-induced water-rock interaction in sandstones. *J Geophys Res Solid Earth*. 1995;100(B7):13093–13112. https://doi.org/10.1029/95JB00912.
53. Ren D, Zhang H, Wang Z, Ge B, Liu D, Zhang R. Experimental study on microscale simulation of oil accumulation in sandstone reservoir. *Front Phys*. 2022;10. https://doi.org/10.3389/fphy.2022.841989.
54. Ren D, Ma L, Liu D, Tao J, Liu X, Zhang R. Control mechanism and parameter simulation of oil-water properties on spontaneous imbibition efficiency of tight sandstone reservoir. *Front Phys*. 2022;10. https://doi.org/10.3389/fphy.2022.829763.
55. Yin H, Zhou W, Dong F, et al. Hydrochemical characteristics and genetic mechanism of porous sandstone geothermal water in northern Jinan, Shandong, China. *Environ Sci Pollut Res Int*. 2024;31(16):24180–24196. https://doi.org/10.1007/s11356-024-32714-2.
56. Su Y, Yang F, Wang B, Jia Z, Duan Z. Reinjection of cooled water into sandstone geothermal reservoirs in China: a review. *Geosci J*. 2018;22(1):199–207. https://doi.org/10.1007/s12303-017-0019-3.
57. Xie J, Yang X, Qiao W, et al. Investigations on CO_2 migration and flow characteristics in sandstone during geological storage based on laboratory injection experiment and CFD simulation. *Gas Science and Engineering*. 2023;117, 205058. https://doi.org/10.1016/j.jgsce.2023.205058.
58. Roesner A, Ikari MJ, Saffer DM, Stanislowski K, Eijsink AM, Kopf AJ. Friction experiments under in-situ stress reveal unexpected velocity-weakening in Nankai accretionary prism samples. *Earth Planet Sci Lett*. 2020;538, 116180. https://doi.org/10.1016/j.epsl.2020.116180.
59. Zhang CY, Hu Z, Elsworth D, et al. Frictional stability of laumontite under hydrothermal conditions and implications for injection-induced seismicity in the gonghe geothermal reservoir, northwest China. *Geophys Res Lett*. 2024;51(10), e2023GL108103. https://doi.org/10.1029/2023GL108103.
60. Chen J, Verberne BA, Spiers CJ. Effects of healing on the seismogenic potential of carbonate fault rocks: experiments on samples from the Longmenshan Fault, Sichuan, China. *JGR*. 2015;120(8):5479–5506. https://doi.org/10.1002/2015JB012051.
61. Barton N, Choubey V. The shear strength of rock joints in theory and practice. *Rock Mech*. 1977;10(1-2):1–54. https://doi.org/10.1007/BF01261801.
62. Barton N. Review of a new shear-strength criterion for rock joints. *Eng Geol*. 1973;7(4):287–332. https://doi.org/10.1016/0013-7952(73)90013-6.
63. Tse R, Cruden DM. Estimating joint roughness coefficients. *Int J Rock Mech Min Sci*. 1997;16(5):303–307. https://doi.org/10.1016/0148-9062(79)90241-9, 1979.
64. Jang H, Kang S, Jang B. Determination of joint roughness coefficients using roughness parameters. *Rock Mech Rock Eng*. 2014;47(6):2061–2073. https://doi.org/10.1007/s00603-013-0535-z.
65. Dieterich JH. Modeling of rock friction: 2. Simulation of preseismic slip. *JGR*. 1979;84(B5):2169–2175. https://doi.org/10.1029/JB084iB05p02169.
66. Ben Zion Y, Rice JR. Slip patterns and earthquake populations along different classes of faults in elastic solids. *JGR*. 1995;100(B7):12959–12983. https://doi.org/10.1029/94JB03037.
67. Marone C, Raleigh CB, Scholz CH. Frictional behavior and constitutive modeling of simulated fault gouge. *JGR*. 1990;95(B5):7007–7025. https://doi.org/10.1029/JB095iB05p07007.
68. Ruina A. Slip instability and state variable friction laws. *JGR*. 1983;88(B12):10359–10370. https://doi.org/10.1029/JB088iB12p10359.
69. Chen J, Verberne BA, Spiers CJ. Interseismic re-strengthening and stabilization of carbonate faults by "non-Dieterich" healing under hydrothermal conditions. *Earth Planet Sci Lett*. 2015;423:1–12. https://doi.org/10.1016/j.epsl.2015.03.044.
70. Im K, Elsworth D, Marone C, Leeman J. The impact of frictional healing on stick-slip recurrence interval and stress drop: implications for earthquake scaling. *JGR*. 2017;122(12):110–117. https://doi.org/10.1002/2017JB014476, 10, 102.
71. Dieterich JH. Modeling of rock friction: 1. Experimental results and constitutive equations. *JGR*. 1979;84(B5):2161–2168. https://doi.org/10.1029/JB084iB05p02161.
72. Ikari MJ, Carpenter BM, Kopf AJ, Marone C. Frictional strength, rate-dependence, and healing in DFDP-1 borehole samples from the Alpine Fault, New Zealand. *Tectonophysics*. 2014;630:1–8. https://doi.org/10.1016/j.tecto.2014.05.005.
73. Marone C. A note on the stress-dilatancy relation for simulated fault gouge. *Pure Appl Geophys*. 1991;137(4):409–419. https://doi.org/10.1007/bf00879042.
74. Tao K, Dang W. Frictional behavior of quartz gouge during slide-hold-slide considering normal stress oscillation. *Int J Coal Sci Technol*. 2023;10(1):14–34. https://doi.org/10.1007/s40789-023-00592-7.
75. Schuster V, Rybacki E, Bonnelye A, Kwiatek G, Schleicher AM, Dresen G. Strain partitioning and frictional behavior of opalinus clay during fault reactivation. *Rock Mech Rock Eng*. 2023;56(3):2065–2101. https://doi.org/10.1007/s00603-022-03129-7.
76. Brown SR, Scholz CH. Closure of random elastic surfaces in contact. *JGR*. 1985;90(B7):5531–5545. https://doi.org/10.1029/JB090iB07p05531.
77. Shen N, Li X, Wang L. Experimental study on frictional properties of fluid-bearing sandstone fractures at different temperatures. *Chin J Theor Appl Mech*. 2023;55(3):744–754. https://doi.org/10.6052/0459-1879-22-400.
78. Tang ZC, Wong LNY. Influences of normal loading rate and shear velocity on the shear behavior of artificial rock joints. *Rock Mech Rock Eng*. 2016;49(6):2165–2172. https://doi.org/10.1007/s00603-015-0822-y.
79. Lockner DA, Summers R, Byerlee JD. Effects of temperature and sliding rate on frictional strength of granite. *Pure Appl Geophys*. 1986;124(3):445–469. https://doi.org/10.1007/BF00877211.
80. Mehrishal S, Sharifzadeh M, Shahriar K, Song J. An experimental study on normal stress and shear rate dependency of basic friction coefficient in dry and wet limestone joints. *Rock Mech Rock Eng*. 2016;49(12):4607–4629. https://doi.org/10.1007/s00603-016-1073-2.
81. Barbot S. A rate-, state-, and temperature-dependent friction law with competing healing mechanisms. *JGR*. 2022;127(11), e2022JB025106. https://doi.org/10.1029/2022JB025106.
82. Verberne BA, van den Ende MPA, Chen J, Niemeijer AR, Spiers CJ. The physics of fault friction: insights from experiments on simulated gouges at low shearing velocities. *Solid Earth*. 2020;11(6):2075–2095. https://doi.org/10.5194/se-11-2075-2020.
83. Rabinowitz HS, Savage HM, Skarbek RM, Ikari MJ, Carpenter BM, Collettini C. *Frictional Behavior of Input Sediments to the Hikurangi Trench, New Zealand. G3*. 2018;19(9):2973–2990. https://doi.org/10.1029/2018GC007633.
84. Kilgore B, Beeler NM, Lozos J, Oglesby D. Rock friction under variable normal stress. *JGR*. 2017;122(9):7042–7075. https://doi.org/10.1002/2017JB014049.
85. Yasuhara H, Marone C, Elsworth D. Fault zone restrengthening and frictional healing: the role of pressure solution. *JGR*. 2005;110(B6). https://doi.org/10.1029/2004JB003327.
86. Dieterich JH, Kilgore BD. Imaging surface contacts: power law contact distributions and contact stresses in quartz, calcite, glass and acrylic plastic. *Tectonophysics*. 1996;256(1-4):219–239. https://doi.org/10.1016/0040-1951(95)00165-4.
87. Bedford JD, Hirose T, Hamada Y. Rapid Fault healing after seismic slip. *JGR*. 2023;128(6), e2023JB026706. https://doi.org/10.1029/2023JB026706.
88. Mclaskey GC, Lockner DA, Kilgore BD, Beeler NM. A robust calibration technique for acoustic emission systems based on momentum transfer from a ball drop. *Bull Seismol Soc Am*. 2015;105(1):257–271. https://doi.org/10.1785/0120140170.
89. Skarbek RM, Savage HM. RSFit3000: a MATLAB GUI-based program for determining rate and state frictional parameters from experimental data. *Geosphere*. 2019;15(5):1665–1676. https://doi.org/10.1130/GES02122.1.
90. Ikari MJ, Carpenter BM, Marone C. *A microphysical interpretation of rate- and state-dependent friction for fault gouge. G3*. 2016;17(5):1660–1677. https://doi.org/10.1002/2016GC006286.